Bioactive Materials 6 (2021) 4163–4175

Contents lists available at ScienceDirect

Bioactive Materials

journal homepage: www.sciencedirect.com/journal/bioactive-materials

In situ bone regeneration with sequential delivery of aptamer and BMP2 from an ECM-based scaffold fabricated by cryogenic free-form extrusion

Tingfang Sun [a,1], Chunqing Meng [a,1], Qiuyue Ding [a], Keda Yu [a], Xianglin Zhang [b], Wancheng Zhang [b], Wenqing Tian [b], Qi Zhang [c], Xiaodong Guo [a,***], Bin Wu [b,**], Zekang Xiong [a,*]

[a] Department of Orthopaedics, Union Hospital, Tongji Medical College, Huazhong University of Science and Technology, Wuhan, 430022, China
[b] State Key Laboratory of Materials Processing and Die & Mould Technology, School of Materials Science and Engineering, Huazhong University of Science and Technology, Wuhan, 430074, China
[c] Wuhan Hi-tech Medical Tissue Research Center, Wuhan, 430206, China

ARTICLE INFO

Keywords:
Bone regeneration *in situ*
Controlled delivery
Cell recruitment
Aptamer
BMP2

ABSTRACT

In situ tissue engineering is a powerful strategy for the treatment of bone defects. It could overcome the limitations of traditional bone tissue engineering, which typically involves extensive cell expansion steps, low cell survival rates upon transplantation, and a risk of immuno-rejection. Here, a porous scaffold polycaprolactone (PCL)/decellularized small intestine submucosa (SIS) was fabricated via cryogenic free-form extrusion, followed by surface modification with aptamer and PlGF-$2_{123\text{-}144}$*-fused BMP2 (pBMP2). The two bioactive molecules were delivered sequentially. The aptamer Apt19s, which exhibited binding affinity to bone marrow-derived mesenchymal stem cells (BMSCs), was quickly released, facilitating the mobilization and recruitment of host BMSCs. BMP2 fused with a PlGF-$2_{123\text{-}144}$ peptide, which showed "super-affinity" to the ECM matrix, was released in a slow and sustained manner, inducing BMSC osteogenic differentiation. *In vitro* results showed that the sequential release of PCL/SIS-pBMP2-Apt19s promoted cell migration, proliferation, alkaline phosphatase activity, and mRNA expression of osteogenesis-related genes. The *in vivo* results demonstrated that the sequential release system of PCL/SIS-pBMP2-Apt19s evidently increased bone formation in rat calvarial critical-sized defects compared to the sequential release system of PCL/SIS-BMP2-Apt19s. Thus, the novel delivery system shows potential as an ideal alternative for achieving cell-free scaffold-based bone regeneration *in situ*.

1. Introduction

The reconstruction of large bone defects is an enormous challenge for both patients and orthopedic surgeons [1]. Three-dimensional (3D) bioprinting, an emerging biofabrication technology, has provided unprecedented opportunities for the treatment of critical-sized bone defects [2–5]. Recently, a variety of 3D-printed materials were developed for bone repair, including metals, ceramics, or polymers such as titanium, hydroxyapatite (HA) and poly (ϵ-caprolactone) (PCL) [6–8]. However, the use of these scaffolds was limited by their inability to mimic the unique microenvironmental cues of the natural bone extracellular matrix [9,10].

Novel biomaterials can provide various structural, mechanical, and biological cues to mobilize endogenous stem cells to the site of injury

Abbreviations: 3D, three-dimensional; Apt19s, aptamer 19s; BMD, bone mineral density; BMP2, bone morphogenic protein 2; BMSC, bone marrow-derived mesenchymal stem cell; CLSM, confocal laser scanning microscopy; CSD, critical-sized calvarial defect; ECM, decellularized matrix; FBS, fetal bovine serum; FDA, US Food and Drug Administration; FITC, fluorescein isothiocyanate; FTIR, Fourier transform infrared; H&E, hematoxylin and eosin; HA, hydroxyapatite; pBMP2, PlGF-$2_{123\text{-}144}$*-fused BMP2; PCL, polycaprolactone; PVDF, polyvinylidene difluoride; Rh6G, rhodamine 6G; SIS, small intestine submucosa; ssDNA, single-stranded DNA.

Peer review under responsibility of KeAi Communications Co., Ltd.

* Corresponding author.
** Corresponding author.
*** Corresponding author.
E-mail addresses: xiaodongguo@hust.edu.cn (X. Guo), wubin19@hust.edu.cn (B. Wu), xzkrunus@163.com (Z. Xiong).

[1] These two authors contributed equally to this work.

https://doi.org/10.1016/j.bioactmat.2021.04.013
Received 13 November 2020; Received in revised form 9 April 2021; Accepted 12 April 2021

and subsequently guide osteogenic differentiation [1,11]. Decellularized matrix (ECM) biomaterials prepared from tissues or organs have become popular for application in bioprinting and regenerative medicine due to their complex components and microstructures of natural extracellular matrices [12,13]. In a previous study, we reported the potential of the small intestinal submucosa (SIS) for use as a novel tissue-derived ECM in bone regeneration, owing to its excellent biocompatibility and ability to induce angiogenesis [9,14]. Thus, SIS gel could represent a novel bio-ink for the construction of 3D scaffolds to repair massive bone defects.

In addition to materials, bioactive molecules induce the recruitment and osteogenic differentiation of bone marrow mesenchymal stem cells (BMSCs) for bone regeneration *in situ*, which involves stimulating the inherent repair mechanisms of the body, inducing host endogenous stem cell recruitment and osteogenic differentiation [15–17]. The homing and osteogenic differentiation of stem cells are sequential events during the process of bone regeneration [18,19]. In this study, to recapitulate the inherent healing cascade, which involves host stem cell mobilization followed by differentiation, a sequential delivery system was designed to actively recruit BMSCs and induce osteogenic BMSC differentiation in two stages.

Aptamers are short, single-stranded DNA (ssDNA) or RNA molecules that can act as targeting ligands for numerous cells [20]. Compared with other targeting agents, such as antibodies, chemokines, growth factors, and peptides, aptamers bind to their target with a high affinity and selectivity, without inducing immunogenic or toxic effects, and exhibit quick circulation clearance [17]. At present, research on nucleic acid aptamers is mainly associated with tumor-targeted therapy, with only a few studies having explored their role in bone regeneration. Recently, a DNA aptamer called Apt19s was developed to specifically recognize pluripotent stem cells. Hu et al. found that Apt19s specifically binds to BMSCs and promotes their migration [21]. Therefore, the functionalization of matrices with Apt19S is likely to be a crucial step in the repair of bone defects, recruiting BMSCs to bone defect areas.

Bone morphogenic protein 2 (BMP2) is one of the most osteoinductive growth factors and has been approved by the US Food and Drug Administration (FDA) for clinical use in the stimulation of osteogenic differentiation of BMSCs [22]. Despite promising results, the application of BMP2 in clinical settings requires high doses, which are associated with severe side effects, including ectopic bone formation, immunological reactions, and tumorigenesis [23–25]. The low efficacy of BMP2 is attributed to two characteristics: firstly, the limited availability of endogenous mesenchymal cells at the site of large bone defects, and secondly, the short half-life of BMP2. Hence, a controllable and sustainable delivery system is required to maintain an effective and safe dosage of BMP2 in the long-term. One recent study reported a domain of placental growth factor 2 (PlGF-$2_{123\text{-}144}$) with "super-affinity" for ECM protein (collagen I, fibronectin, etc.). *In vivo*, PlGF-$2_{123\text{-}144}$ fused growth factor was strongly retained in ECM protein, hence overcoming the burst release and rapid degradation of growth factors [26]. Thus, PlGF-$2_{123\text{-}144}$-fused BMP2 (pBMP2) is a good candidate for the controlled release profile required in ECM-derived SIS bio-ink.

In this study, we designed an ECM-based scaffold with the capability to sequentially release Apt19s, followed by the release of pBMP2 in a controlled manner. Here, ECM-derived SIS was used for its excellent biocompatibility, ability to induce angiogenesis [9,14], and affinity to pBMP2 [26]. In addition, PCL was applied as the mechanical support. After PCL and SIS were fabricated as a 3D scaffold by cryogenic free-form extrusion, Apt19s and pBMP2 were coated on PCL/SIS to form a PCL/SIS-pBMP2-Apt scaffold. Thus, we hypothesize that PCL/SIS provided a platform for the sequential release of Apt19s and pBMP2, and efficiently promoted cell recruitment and differentiation, thus achieving cell-free bone regeneration (Scheme 1).

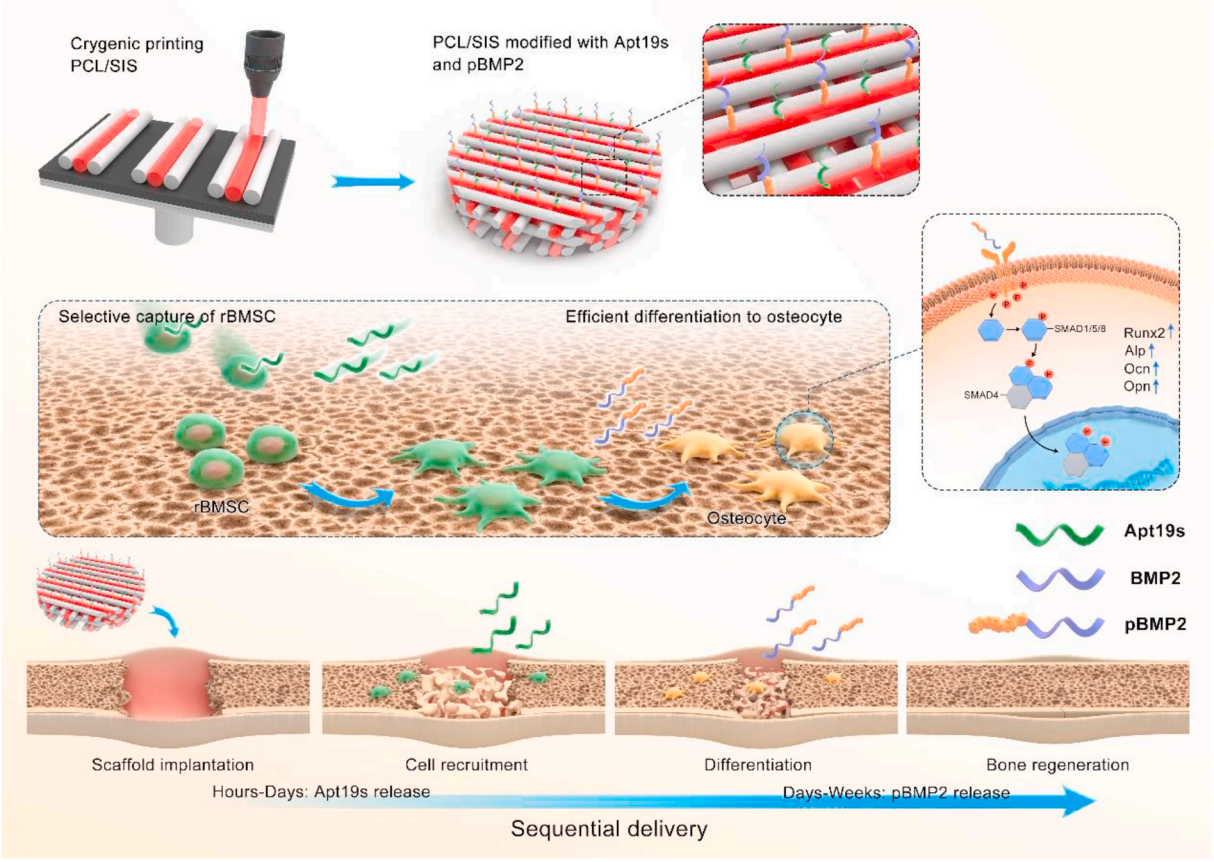

Scheme 1. Schematic illustrations of *in situ* bone regeneration with sequential delivery of aptamer and BMP2 from an ECM-based scaffold fabricated by cryogenic free-form extrusion.

2. Materials and methods

2.1. Fabrication of PCL/SIS-pBMP2-Apt scaffolds

pBMP2, BMP2/PlGF-$2_{123\text{-}144}$*-fused BMP2, was synthetized by GenScript Biotechnology Co., Ltd (Nanjing, China) using the mammalian expression system of HEK-293E cells, according to the method outlined in a previous study [26]. At 7 d post-transfection, the cell culture medium containing pBMP2 was transferred into a HisTrap HP 5-mL column for elution. Fractions of proteins were analyzed by SDS-PAGE, and any fractions containing pBMP2 were harvested and further dialyzed against PBS overnight. The concentration of pBMP2 was determined using ELISA (R&D Systems, Minneapolis, MN, USA), and the purity of pBMP2 was verified as >99% by SDS-PAGE and MALDI-TOF.

Aptamer 19s (Apt19s) was synthesized using an ABI3400 DNA/RNA synthesizer (Applied Biosystems, Foster City, CA, USA). The as-synthesized Apt19s was then purified by high-performance liquid chromatography (Agilent, 1260 GC, Santa Clara, CA, USA) using a C-18 column: Apt19s (5′-AGGTCAGATGAGGAGGGGGACTTAGGACTGGG TTTATGACCTATGCGTG-3′); FITC-labeled Apt19s (5′-AGGTCA-GATGAGGAGGGGGACTTAGGACTGGGTTTATGACCTATGCGTG-FITC-3′); Amino-modified Apt19s (5′-NH2-(A)9-AGGTCAGATGAGGA GGGGGACTTAGGACTGGGTTTATGACCTATGCGTG-3′).

The SIS slurry was prepared according to the method of a previous study [27]. Briefly, 0.3 g SIS powder (Sun Shing Biotechnology Co., Ltd., Guangzhou, China) was dissolved in 10 mL 0.01 M hydrochloric acid with the addition of 0.03 g pepsin solution. This mixture was stirred constantly for 36 h at 37 °C. The resulting slurry was centrifuged to remove residual fragments and air bubbles.

Two PCL printing modes, including cryogenic and melting printings, were tested. For cryogenic printing, PCL slurry was prepared by adding 4 g of PCL pellets (MW ~80,000; Perstorp UK Limited, Warrington, UK) into 6 mL of glacial acetic acid. The resulting mixture was magnetically stirred for 6 h at 65 °C. Subsequently, the solution was centrifuged at 2000 rpm for 2 min to remove any bubbles. In addition, melting printing was also conducted as a control group, in which PCL pellets were placed into the barrel and heated to 110 °C.

Before cryogenic printing, PCL and SIS slurries were loaded into separate 10-mL syringes. Hybrid scaffolds (20 × 20 × 1 mm, Ø8 mm × 2 mm) were fabricated on a two-nozzle 3D printing system (MAM-II, Fochif, China) installed with a home-designed cryogenic substrate. The substrate was cooled at −20 °C to achieve rapid solidification during printing. In each layer of the scaffolds, PCL slurry was firstly extruded through a motor-driven piston with an extrusion speed of 0.006 mm/s and printed in the form of a skeleton, with a pore size of ~350 μm. Then, the SIS slurry was deposited pneumatically and used to fill the vacancy between every two PCL filaments with one line gapped (air pressure: 12 kPa). 22G nozzles were utilized on the syringes. The platform speed was set at 8 mm/s. After printing, the scaffolds were immediately placed under lyophilization for 36 h.

To coat the Apt19s and pBMP2 on the prepared PCL/SIS scaffold, the scaffold was immersed in 100 mL of activation buffer (0.1 M MES, pH 6). Then, the carboxyl groups on the surface of SIS were activated by adding 1 g of 1-ethyl-3-(3-dimethylaminopropyl) carbodiimide and 12 mg of N-hydroxysuccinimide for 15 min at room temperature. The activation buffer was removed, and the material was washed with the coupling buffer (0.1 M PBS, pH 7.2) twice before adding 2 mL of PBS. 4 nmol of amino-modified Apt19s and a specific quantity of PlGF-$2_{123\text{-}144}$-BMP2 (pBMP2, 20 ng for cell culture, 2 μg for animal experiments) were added and reacted for 12 h in a reciprocating oscillator. The aptamer and pBMP2-modified scaffolds were purified by washing with coupling buffer twice. This procedure was finished with another freeze-drying for 36 h.

In the same way, PCL/SIS, PCL/SIS-Apt, PCL/SIS-Apt-BMP2, and PCL/SIS-Apt-pBMP2 scaffolds were fabricated. All scaffolds were sterilized with ethylene oxide at 37 °C.

2.2. Characterization of scaffolds

Rheological measurements of the prepared SIS slurry were performed using a DHR rheometer (TA Instruments, New Castle, DE, USA) with two parallel plates. The viscosity of the dSIS slurry was tested under a flow ramp, with a duration time of 300 s and a shear rate ranging from 0.01 to 1000 s^{-1} with a linear increment. The storage modulus (G′) and loss modulus (G″) were recorded as a function of frequency through oscillatory measurements under 1 Pa and frequency from 0.1 to 10 Hz.

The micromorphology of the 3D-printed scaffolds was observed under a field emission scanning electron microscope (JSM7600F; JEOL Ltd, Tokyo, Japan). Before conducting the experiments, the samples were gold-coated for 200 s to increase their electro-conductivity. The X-ray diffraction (XRD) patterns of cryogenic-printed and melting-printed scaffolds were acquired via an X-ray diffractometer (XRD-6100, Shimadzu, Kyoto, Japan) using CuKα radiation with a diffraction angle of 2θ = 5–60° at a scanning speed of 5°/min. Fourier transform infrared (FTIR) spectroscopy was performed using an FTIR instrument (Nicolet iS5, Thermo Fisher Scientific, Waltham, MA, USA), with a spectral range of 4000–500 cm^{-1} and a resolution of 0.5 cm^{-1}).

To confirm the successful loading of pBMP2 and Apt on scaffolds, Rhodamine 6G (Rh6G) and fluorescein isothiocyanate (FITC) were respectively used to label Apt-19s and pBMP2 to monitor the drug distribution. The scaffolds modified with Apt19s and pBMP2 were observed under confocal laser scanning microscopy (CLSM).

2.3. In vitro release study

The scaffolds were dispersed in 10 mL of PBS buffer. Aliquots were taken from the solution at each predetermined time point (3 h, 12 h, 24 h, 4 d, 7 d, 10 d, 13 d, 19 d, 25 d, and 31 d). Rh6G was used as a model guest molecule to monitor the release kinetics of Apt19s. The release of the Rh6G-Apt19s suspensions was quantified at a wavelength of 527 nm using a multi-detection microscope reader (BioTeck Instruments, Winooski, VT, USA). The BMP2 concentrations were quantified with a BMP2 ELISA kit (R&D Systems) according to the manufacturer's instructions. The cumulative release ratio was calculated as the ratio of the cumulative mass of BMP2 released at each time interval to the total BMP2 in the scaffold. The total BMP2 loaded into the scaffolds was measured by dissolving scaffolds in 1 mM HCL.

2.4. Cell culture

Rat bone marrow stromal stem cells (rBMSCs) were purchased from the China Center for Type Culture Collection (Wuhan University, Hubei, China) and maintained in a basal growth medium composed of DMEM supplemented with 10% fetal bovine serum (FBS). The osteogenic induction medium for rBMSCs consisted of basal growth medium supplemented with 100 nM dexamethasone, 10 mM beta-glycerophosphate, and 0.05 mM ascorbic acid. Cells were cultured in a humidified atmosphere containing 5% CO_2 at 37 °C, and the medium was replenished every 2 d. The cells were sub-cultured prior to confluence, and cells from passage 4 were used for this study.

2.5. Cell proliferation

The proliferation of rBMSCs on scaffolds was quantified using the BrdU Cell Proliferation Assay Kit (Roche, Basel, Switzerland), as previously described [14]. The rBMSCs were seeded on the PCL/SIS, PCL/SIS-Apt, PCL/SIS-BMP2-Apt, and PCL/SIS-pBMP2-Apt scaffolds at a density of 2×10^5 cells/scaffold in 96-well tissue plates and cultured in a growth medium for 1, 3, 5, and 7 d. At each time point, the scaffolds with adherent cells were transferred to a new 96-well plate and washed with PBS twice. Subsequently, BrdU solution was added to the specimens and incubated at 37 °C for 4 h. After fixing for 30 min at 37 °C, the specimens were incubated with antiBrdU-peroxidase solution for 2 h.

Substrate solution was then added to observe the color reaction after rinsing with PBS. After stopping the reaction, the absorbance was measured at a wavelength of 450 nm using a microplate reader (Thermo LabSystems, Waltham, MA, USA).

2.6. Cell viability

CLSM was used to quantify the cell viability after culture for 3 and 7 d. The cell-seeded scaffolds were washed with PBS and stained with 60 μL double-staining solution containing 2 μM Calcein-AM and 4 μM propidium iodide. Subsequently, the amount and distribution of cells on the MBG/SF scaffold were observed using a confocal laser scanning microscope (Nikon, Tokyo, Japan) equipped with a digital camera. Images were obtained from five randomly chosen fields to quantify the percentage of live cells: P = number of live cells/(number of live cells + number of dead cells). Three specimens for each group (n = 3) yielded 15 images for each time point.

2.7. Cell morphology

A 6-well transwell system (Corning, New York, USA) was employed to investigate the effect of scaffolds on cells. Briefly, rBMSCs were seeded into the lower chambers at a density of 1×10^5 cells/well. The scaffold was placed in the upper chamber for 7 h. After 7 h of culture, the fixed and permeabilized rBMSCs were stained with DAPI to visualize the nucleus and phalloidin to visualize the cytoskeleton (F-actin) at 37 °C for 1 h. After washing with PBS 3 times, the cells were observed under CLSM.

2.8. Migration of scaffold effect on rBMSCs

The capacity of the effect of the scaffolds on rBMSC recruitment was assessed using a transwell system (Costar, 24-well plate, 8 μm). Briefly, 2×10^4 cells in 100 μL of medium containing 1% FBS were seeded into the upper chambers of the transwell system. The scaffold with 700 μL of DMEM containing 10% FBS was placed in the lower chamber for 24 h. After incubating for 24 h, the chambers were washed with PBS and fixed in 4% polyoxymethylene for 20 min. After air drying, the filters were stained with crystal violet. The cell number was determined using an optical microscope. All experiments were performed in triplicate on three independent occasions.

2.9. In vitro osteogenic ability of rBMSCs on different scaffolds

2.9.1. Alkaline phosphatase staining and quantitative analysis

A total of 2×10^5 rBMSCs was seeded on the PCL/SIS, PCL/SIS-Apt, PCL/SIS-BMP2-Apt, and PCL/SIS-pBMP2-Apt scaffolds ($1 \times 1 \times 0.2$ cm^3) in a 24-well plate. After osteogenic induction for 7 and 14 d, ALP staining was performed using a BCIP/NBT ALP color development kit (Beyotime Biotechnology, Nanjing, China), according to the manufacturer's instructions. Meanwhile, ALP activity was quantitatively determined using a SensoLyte PNPP Alkaline Phosphatase Assay kit (Beyotime Biotechnology). The double-stranded DNA (dsDNA) concentration in each sample was quantified using a PicoGreen dsDNA Assay Kit (Invitrogen, Carlsbad, CA, USA), and the ALP activity of each sample was normalized to the dsDNA concentration.

2.9.2. Calcium nodule deposition evaluation

Alizarin Red S staining was used to display the ECM mineralized nodule formation. Briefly, 2×10^5 rBMSCs were seeded on the PCL/SIS, PCL/SIS-Apt, PCL/SIS-BMP2-Apt, and PCL/SIS-pBMP2-Apt scaffolds and cultured in osteogenic medium for 21 d. After osteogenic induction of 14 and 21 d, the cells/scaffolds were stained with 1 wt% alizarin red (pH 4.2) according to the manufacturer's instructions. For the quantification of calcium nodule deposition, mineralized nodule staining was dissolved in 10% (v/v aqueous solution) cetylpyridinium chloride monohydrate. The absorbance of the extract was determined spectrophotometrically at 620 nm.

2.10. Real-time PCR

After culture for 3, 7 and 14 d, the total RNA from 2×10^5 cells seeded on scaffolds ($1 \times 1 \times 0.2$ cm^3) was extracted using Trizol reagent (Thermo Fisher Scientific). The quantity of total RNA was determined by spectrophotometry. Complementary DNA was synthesized using a PrimeScript reagent Kit (Takara Bio, Shiga, Japan) according to the manufacturer's instructions. Real-time polymerase chain reaction was performed on a 96-well plate ABI Prism 7500 (Applied Biosystems, Foster City, CA, USA) using a KAPA SYBR FAST qPCR Kit Master Mix (KAPA Biosystem, Boston, USA). Ct values were normalized to the relative expression, which was calculated using the $2^{-\Delta\Delta Ct}$ method normalized to GAPDH. Primers for osteogenic genes encoding Ocn, Runx2, ALP, and Opn are listed in Table 1.

2.11. Western blot

To examine the effect of scaffolds on protein expression levels, total proteins were extracted from the cells/scaffolds after being cultured for 7 d. Subsequently, cell lysates were centrifuged at 14,000×*g* at 4 °C for 15 min to harvest supernatant protein samples, which were then transferred onto a polyvinylidene difluoride (PVDF) membrane. The PVDF membrane was then blocked with 5% (w/v) dried milk in TBST for 1 h, and the membranes were incubated with primary antibodies against phosphorylated-Smad1/5/8 (*p*-Smad1/5/8, Abcam, ab92698), RUNX2 (Abcam, ab23981), OCN (Abcam, ab93876), and β-actin (Abcam, ab8226) overnight at 4 °C with gentle shaking. The membranes were rinsed five times with TBST buffer for 5 min and incubated with anti-rabbit IgG-HRP conjugate secondary antibody (Santa Cruz Biotechnology, Dallas, TX, USA) for 1 h at room temperature. Finally, the protein bands on the PVDF membrane were detected using an enhanced chemiluminescence detection system (Beyotime Biotechnology).

2.12. Animal experiments

All animal procedures were performed in accordance with the Guideline for the Care and Use of Laboratory Animals of Huazhong University of Science and Technology (HUST) and were approved by the Animal Care and Use Committee at Tongji Medical College, HUST. Sprague Dawley rats (40 males; 180–200 g) were used to model a critical-sized calvarial defect (CSD). All surgical procedures were performed on anesthetized rats (chloraldurate 1 mL/kg, administered intraperitoneally). A 1.5 cm incision was made on the scalp in the sagittal direction. A CSD with a diameter of 8 mm was created using a trephine bur and implanted with scaffolds (Ø8 × 2 mm). The animals were randomly divided into 4 groups: PCL/SIS (n = 5), PCL/SIS-Apt (n = 5), PCL/SIS-BMP2-Apt (n = 5), and PCL/SIS-pBMP2-Apt (n = 5). The animals were sacrificed at 4 and 8 weeks after implantation surgery to explant the cranium for analysis.

Table 1
PCR primers for genes encoding Runx2, Opn, Ocn, ALP, and GAPDH.

Primer	Forward	Reverse
GAPDH	F5′-GACAAAATGGTGAAGGTCGGT	R5′-GAGGTCAATGAAGGGGTCG
Runx2	F5′-AACTTGCTAACGTGAATGGTC	R5′-TAGCCCACTGAAGAAACTTGG
Opn	F5′-GAGGTGATAGCTTGGCTTACGG	R5′-ACGCTGGGCAACTGGGAT
Ocn	F5′-GAACAGACAAGTCCCACACAG	R5′TCAGCAGAGTGAGCAGAAAGAT
ALP	F5′-ACCACCACGAGAGTGAACCA	R5′-CGTTGTCTGAGTACCAGTCCC

2.12.1. Micro-CT analysis of bone defects

The specimens were scanned on a micro-CT scanner (SkyScan 1176 X-ray microtomography; Bruker, Billerica, MA, USA) at a resolution of 18 μm to assess bone regeneration at the defect site on the cranium. After 3D reconstruction, CT-analyzer software (Bruker, Billerica, MA, USA) was used to analyze the bone mineral density (BMD) and the percentage bone volume (bone volume/tissue volume, BV/TV) (n = 5).

2.12.2. Histological assessment

The specimens were fixed in 10% neutral formalin and subsequently decalcified in EDTA (pH 7.0) at 4 °C. The completely decalcified specimens were embedded in paraffin and sectioned into 5-μm-thick slices. For histological analysis, the sections were stained with hematoxylin and eosin (H&E) and Masson for microscopic observation. Semi-quantitative image analysis of H&E-stained sections from each group (n = 5) was performed with Image-Pro Plus software (Media Cybernetics, Rockville, MD, USA) to assess the new bone fractions in the defects. Meanwhile, the new vessel density was determined from the number of new blood vessels in the defect area divided by the entire defect area.

2.13. Statistical analysis

All experiments were performed in triplicate, unless specifically stated. All numerical data were expressed as the mean ± standard deviation. Statistical significance was tested via analysis of variance followed by Tukey's post-hoc test, with $p < 0.05$ considered statistically significant.

3. Results

3.1. Scaffold characterization

As shown in Fig. 1A, the two PCL scaffold groups had obviously different morphologies. The cryogenic-printed PCL structs had micro pores on the surface, while melting-printed PCL structs possessed a compact surface without pores. In addition, the fiber widths of the cryogenic-and melting-printed scaffolds were 419.8 ± 21.4 μm and 567.9 ± 42.8 μm, respectively; while the pore sizes of cryogenic- and melting-printed scaffolds were 269.1 ± 23.8 μm and 207.4 ± 25.7 μm, respectively. In other words, the cryogenic-printed scaffold possessed a smaller fiber width and bigger pore size compared to the melting-printed scaffold. Through the cross-sectional view in Fig. S1, this conclusion was confirmed again: the melting-printed filament was flatter than the cryogenic-printed one. Furthermore, the SIS fiber was much thinner than the PCL struct, and the intervals between filaments in the cryogenic printing group are much bigger than those in the melting printing group. Furthermore, the SIS filaments shrank to thin films, and in the cryogenic-printed scaffold, two layers of SIS films were observed clearly. However, in the melting-printed scaffolds, the melted PCL structs collapsed, so only one layer of SIS film was observed. In addition, the SIS film area in the cryogenic group was bigger than the one in the melting printing group due to the different interval sizes. Considering the different sizes of pores between scaffold structs and struct surfaces, PCL/SIS had a hierarchical porous network with pore diameters ranging from dozens of microns to hundreds of micrometers.

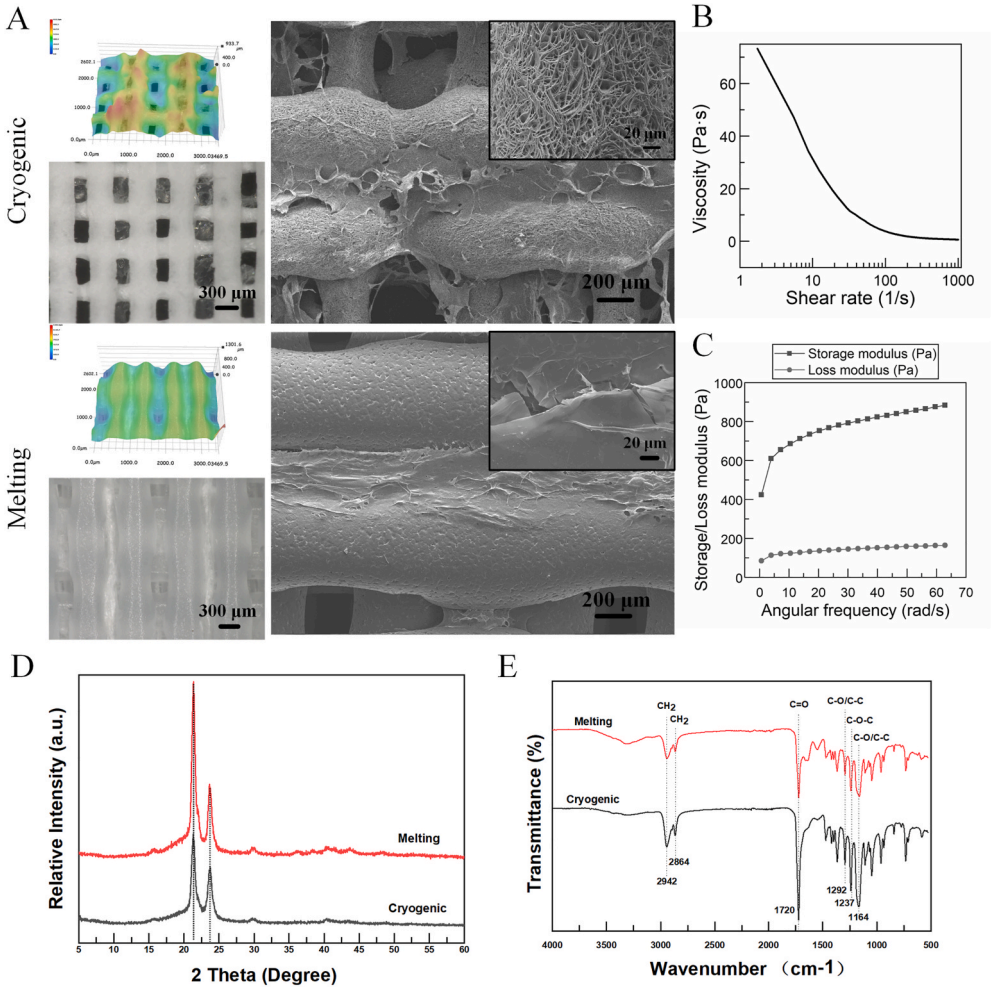

Fig. 1. (A) Morphologies of cryogenic-printed and melting-printed PCL/SIS scaffolds observed using super deep optical microscope and SEM. (B–C) The rheological properties of prepared SIS slurry. (D–E) XRD and FTIR patterns of cryogenic-printed and melting-printed PCL/SIS scaffolds.

The rheological properties of the SIS slurry were measured to evaluate its flow behavior, i.e. whether or not it was coherent with the requirements for printing, and the results are shown in Fig. 1B and C. The results showed that the storage modulus (G′) was bigger than the loss modulus (G″), indicating a solid-like state of SIS slurry. Furthermore, a remarkable shear thinning behavior was observed in the measured shear rate range. Fig. 1D shows similar XRD patterns for cryogenic- and melting-printed PCL/SIS scaffolds. It shows that the typical peaks reflecting (110) and (111) crystal planes of PCL were found at around 2θ = 21.7° and 22.3°, respectively. These peaks matched well with the previous studies [28]. The pure SIS contained uncrystallized proteins such as collagen; therefore, no obvious peaks were found on the SIS curve. As shown in Fig. 1E, both samples have sharp strong peaks at 1720 cm^{-1}, which is the stretching vibration peak of C═O in PCL. The peak at 2942 cm^{-1} is related to the asymmetric stretching vibration of CH_2, and the peak at 2864 cm^{-1} is related to the symmetric stretching vibration of CH_2. The peak at 1292 cm^{-1} represents the stretching vibration of C–O and C–C in the PCL crystalline phase, while the peak at 1164 cm^{-1} represents the stretching vibration of C–O and C–C in the amorphous phase of PCL. In addition, the peak at 1237 cm^{-1} represents the C–*O*–C asymmetric stretching vibration. These peaks matched well with the previous studies [29]. These results indicate that the melting and cryogenic printing methods provide negligible influence on the main function groups in PCL.

3.2. In vitro release of Apt19s and pBMP2

As shown in Fig. 2A, the red fluorescence indicating Apt19s and the green fluorescence indicating pBMP2 were uniformly distributed on the surface of their respective scaffolds. The release profiles of Apt19s and BMP-2 from the scaffolds of PCL/SIS-BMP2-Apt and PCL/SIS-pBMP2-Apt are shown in Fig. 2B and C. Apt19s released from PCL/SIS-pBMP2-Apt showed a burst release in the first day (42.46%), which subsequently slowed down, with approximately 87.46% of the total Apt19s released after 7 d. The release of BMP2 from PCL/SIS-BMP2-Apt without $PlGF\text{-}2_{123\text{-}144}$ treatment showed a fast release (74.44%) over 7 d, similar to Apt19s. In contrast, the release of BMP2 from PCL/SIS-pBMP2-Apt in the presence of $PlGF\text{-}2_{123\text{-}144}$ occurred in a steady and sustained manner compared with Apt19s. A minor burst of 16.87% of the total BMP2 was released on the first day, followed by the long-term release of the remaining BMP2 over the subsequent four weeks. At 10 d, almost 90.59% of the Apt19s was released from the PCL/SIS-pBMP2-Apt scaffold. At this stage, over 40% of BMP2 remained, indicating the sequential release behavior of Apt19s and BMP2 from the PCL/SIS-pBMP2-Apt scaffold.

3.3. Proliferation, viability, and morphology of rBMSCs cultured with scaffolds

The proliferation of rBMSCs on scaffolds was assessed using the BrdU assay (Fig. 3). rBMSCs were found to proliferate well on the four kinds of scaffolds over a period of 7 d. However, the cells exhibited a higher proliferation on the PCL/SIS-BMP2-Apt and PCL/SIS-pBMP2-Apt scaffolds compared to the PCL/SIS-Apt and PCL/SIS scaffolds during culturing. It is worth noting that the rBMSCs on the PCL/SIS-BMP2-Apt scaffold showed slightly higher proliferation rates compared to those on

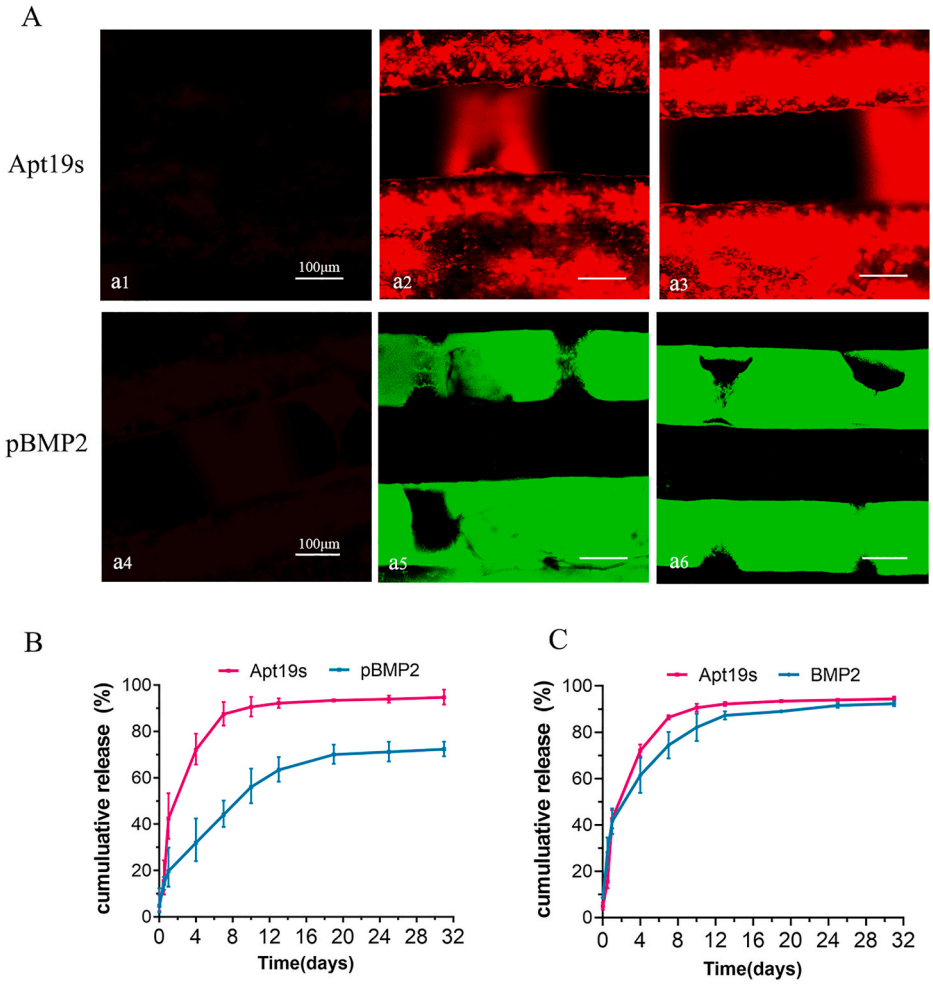

Fig. 2. The loading and release profiles of Apt19s and BMP2. (A) Confocal microscopy images of the PCL/SIS scaffold modified with Apt19s and pBMP2. The upper line showed the confocal microscopy images of the PCL/SIS scaffold without Apt19s (a1), modified 2 nmol (a2) and 4 nmol (a3) of rhodamine-labeled Apt19s. The upper line showed the confocal microscopy images of the PCL/SIS scaffold without pBMP2 (a4), modified 1 μg (a5) and 2 μg (a6) of FITC-labeled pBMP2. (B–C) In vitro release profiles of Apt19s and BMP-2 from scaffolds of PCL/SIS-pBMP2-Apt and PCL/SIS-BMP2-Apt.

the PCL/SIS-pBMP2-Apt scaffold from the 3rd to 5th day ($p > 0.05$). However, this difference was reversed after 7 d. The sustained release maintained an effective dosage on cell proliferation over time. Moreover, no significant differences in cell proliferation on the PCL/SIS-Apt and PCL/SIS scaffolds were detected. These results indicate that the aptamer did not significantly affect cell proliferation, consistent with previous research [20,30].

The live/dead assay results of the rBMSCs on the scaffolds are shown in Fig. 4. Live cells stained with calcein-AM (green) appeared to adhere to the surfaces of the scaffolds (Fig. 4A). The percentage of live cells (Fig. 4B) was approximately 90%, with minor variations observed among the different groups. This indicated that all kinds of scaffolds promote cell adhesion and proliferation. The live cell density was significantly increased in the PCL/SIS-BMP2-Apt and PCL/SIS-pBMP2-Apt groups compared to that in the PCL/SIS or PCL/SIS-Apt groups ($p < 0.05$), while no obvious difference in live cell density was observed between PCL/SIS-BMP2-Apt and PCL/SIS-pBMP2-Apt scaffolds. The live cell density in the PCL/SIS-Apt group was almost equal to that in the PCL/SIS group. These results were in accordance with the BrdU assay.

After cells were cultured for 7 h, significant differences in cell morphology between PCL/SIS and Apt-treated scaffolds were observed. In the PCL/SIS group, the strong staining of the actin cytoskeleton showed unstretched and amoeboid rBMSCs, while rBMSCs in the Apt-treated scaffolds exhibited a well-spread, dendritic structure in the cytoskeleton. Therefore, the incorporation of Apt19s effectively promoted cell adhesion and spread.

3.4. Migration of rBMSCs

The migration of BMSCs was evaluated *in vitro* using a transwell system. As shown in Fig. 5, cell migration across the membrane of a chamber was confirmed by the release of Apt19s from the scaffold. The number of migrated rBMSCs in the groups containing Apt19s was significantly higher than in the control ($p < 0.05$), while the number of migrated BMSCs in Apt19s- and BMP-2-loaded scaffolds was slightly higher than that in scaffolds loaded with Apt19s alone ($p > 0.05$).

3.5. Osteogenic differentiation analysis

ALP is a marker of early stage osteogenic differentiation. The ALP staining results are shown Fig. 6. Moreover, the 7 and 14 d results indicated that the reaction color intensified with time. Compared to the control scaffold and the scaffold containing only Apt19s, the scaffold containing BMP2 was found to significantly promote ALP production, shown by the deeper, bluer color response. Quantitative analysis of the ALP further confirmed this phenomenon (Fig. 6B). ALP activity was significantly elevated in the PCL/SIS-pBMP2-Apt group compared to that in the PCL/SIS-BMP2-Apt group. However, little difference was observed between the PCL/SIS and PCL/SIS-Apt scaffolds, indicating that Apt had no effect on early osteogenic differentiation.

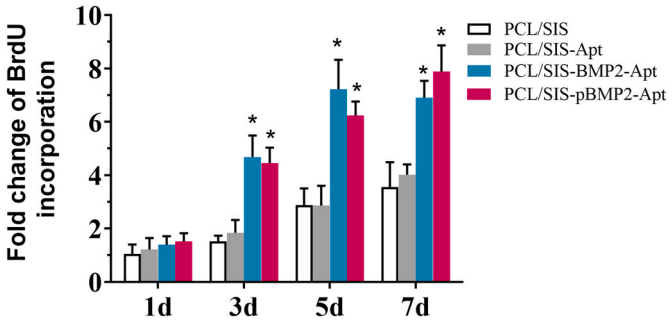

Fig. 3. The fold change of BrdU incorporation after culturing for 1, 3, 5, and 7 days. Statistical significance compared to the PCL/SIS group is indicated by *$p < 0.05$.

Calcium nodule deposition is a marker of late-stage osteogenic differentiation. The scaffold containing BMP2 showed more mineral formation than the PCL/SIS and PCL/SIS-Apt scaffolds (Fig. 6C) ($p < 0.05$). Moreover, PCL/SIS-pBMP2-Apt exhibited significant more mineral nodules than PCL/SIS-BMP2-Apt ($p < 0.05$). However, differences in mineral nodules between the PCL/SIS and PCL/SIS-Apt groups were not significant ($p > 0.05$).

The expression levels of osteogenic genes, including *Alp*, *Runx2*, *Alp*, *Ocn*, and *Opn*, are shown in Fig. 7E. Scaffolds with BMP2 exhibited a significantly upregulated expression of these genes compared to that in those without BMP2. The PCL/SIS-pBMP2-Apt scaffold showed the highest level at each time point. The scaffolds containing Apt19s only slightly improved the expression level of these genes compared to the control group ($p > 0.05$). No obvious differences in the expression levels of these genes were observed between the PCL/SIS-BMP2-Apt and PCL/SIS-pBMP2-Apt groups at day 3. However, the expression level of those genes in the PCL/SIS-pBMP2-Apt group was significantly higher at days 7 and 14. These results demonstrate that the promotion effect of the PCL/SIS-pBMP2-Apt was exerted at a later stage of osteogenic differentiation.

As shown in Figs. 6F and 2S, the expression levels of osteogenic-related proteins (RUNX2 and OCN) were significantly increased in rBMSCs on the PCL/SIS-pBMP2-Apt scaffold compared to those in PCL/SIS-BMP2-Apt or PCL/SIS-Apt scaffolds at day 7. No significant difference was found between PCL/SIS-Apt and PCL/SIS scaffolds. The Western blot results of the osteogenesis-related proteins (OCN, RUNX2) after 7 d was observed to be in accordance with the RT-qPCR analysis. Additionally, the level of the canonical Smad signaling molecule (*p*-Smad1/5/8) was obviously elevated in the PCL/SIS-pBMP2-Apt and PCL/SIS-BMP2-Apt groups compared to the PCL/SIS-Apt and PCL/SIS scaffolds. The PCL/SIS-pBMP2-Apt group showed the highest *p*-smad1/5/8 expression level.

3.6. In vivo studies

The representative 3D-rendering images of the rat calvarial are shown in Fig. 7A. Substantial mineralized tissue was observed in defects implanted with PCL/SIS-BMP2-Apt and PCL/SIS-pBMP2-Apt scaffolds at 4 and 8 weeks post-surgery. In contrast, PCL/SIS and PCL/SIS-Apt groups showed largely open and minimally mineralized regions in the center of the defect or on regions confined mostly to the defect edges. Interestingly, the mineralized tissue at the center of defects was distributed in a grid pattern, while the PCL grid guided mineralization and new bone formation. Using micro-CT analysis, the BV/TV% and BMD values for the PCL/SIS-Apt group were found to be significantly higher than those in the control group (Fig. 7B). These results demonstrate that scaffolds containing aptamers only stimulated bone regeneration *in vivo*, which may be attributed to the stimulatory effect of Apt19s on the homing of stem cells. The BV/TV% and BMD values for the PCL/SIS-pBMP2-Apt group were significantly higher than those for the PCL/SIS-BMP2-Apt group, and indicated that the control group released increasing levels of BMP2 in the new bone volume.

The results of the histological examination are shown in Fig. 8. As shown in the panoramic view of the coronal section of HE staining, the bone completely bridged the injury site on the PCL/SIS-pBMP2-Apt scaffold by 8 weeks post-surgery, whereas, at the same time point, PCL/SIS-BMP2-Apt and PCL/SIS-Apt groups were filled with few bone islands and multiple connective tissue islands. On the other hand, the PCL/SIS scaffold was mainly filled with connective tissue. Under high magnification, newly formed bone (indicated by NB) accompanied by newly formed vessels were observed inside the PCL/SIS-pBMP2-Apt scaffolds. None of the rats showed evidence of an inflammatory or immune response, despite the use of porcine-derived SIS, thus confirming the biocompatibility of the constructs. As shown in Fig. 8 B and C, the histological quantitative analysis indicated that the PCL/SIS-pBMP2-Apt

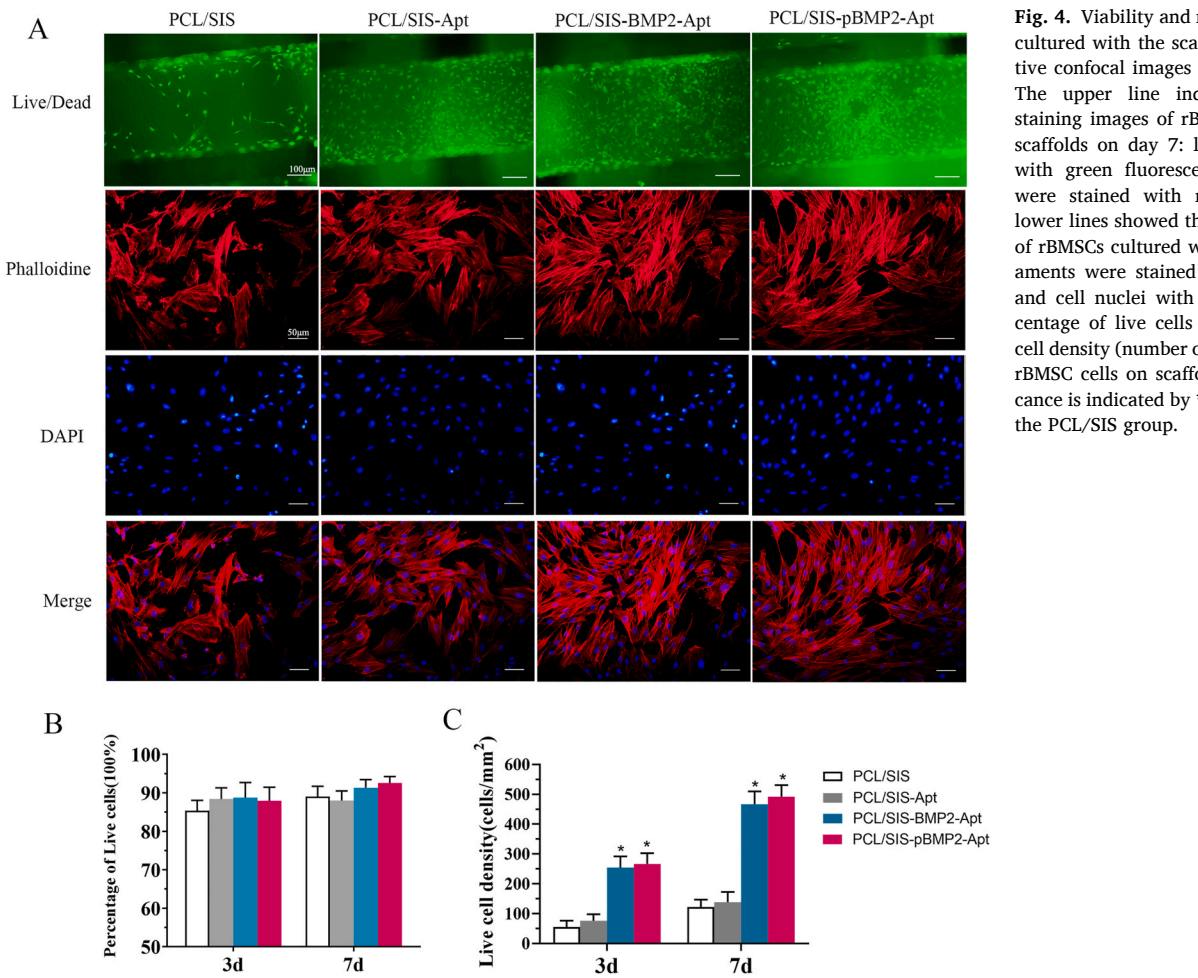

Fig. 4. Viability and morphology of rBMSCs cultured with the scaffolds. (A) Representative confocal images of cells with scaffolds. The upper line indicates the live/dead staining images of rBMSC cells cultured on scaffolds on day 7: live cells were stained with green fluorescence while dead cells were stained with red fluorescence. The lower lines showed the cytoskeletal staining of rBMSCs cultured with scaffolds: actin filaments were stained with phalloidin (red) and cell nuclei with DAPI (blue). (B) Percentage of live cells on scaffolds. (C) Live cell density (number of live cells per mm^2) of rBMSC cells on scaffolds. Statistical significance is indicated by $*p < 0.05$ compared to the PCL/SIS group.

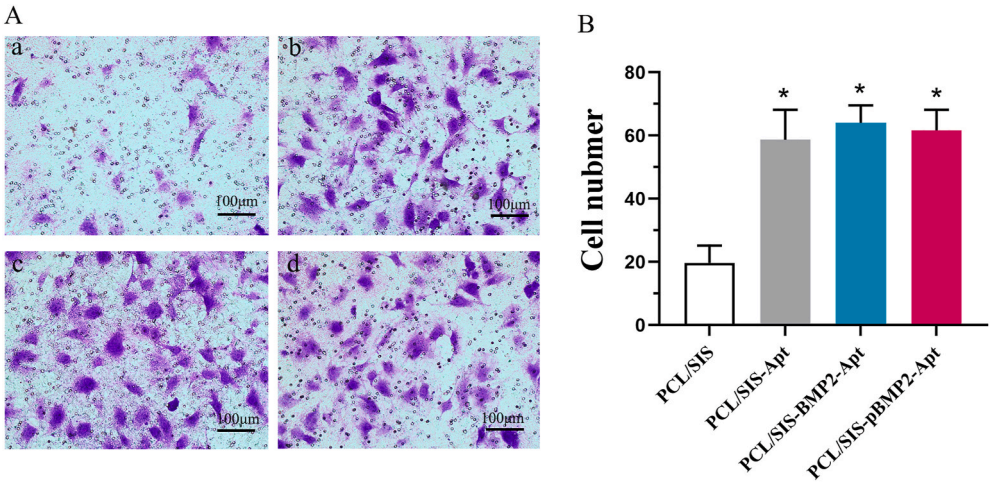

Fig. 5. (A) Representative photos of cell migration in scaffold groups. (B) The numbers of migrating cells were determined. Statistical significance is indicated by $*p < 0.05$ compared to PCL/SIS group.

group had the highest new bone area fraction compared with the PCL/SIS-BMP2-Apt group at 4 and 8 weeks. Meanwhile, the PCL/SIS-pBMP2-Apt scaffold significantly improved newly formed vessel amounts compared with PCL/SIS-BMP2-Apt and PCL/SIS-Apt groups ($p < 0.05$).

4. Discussion

In situ tissue engineering is a powerful strategy for the treatment of bone defects; in this strategy, biomaterials are designed to mobilize endogenous stem cells to the site of injury and provide a highly osteoinductive environment [17,31]. In this study, we developed an ECM-based scaffold loaded with bioactive molecules to induce bone

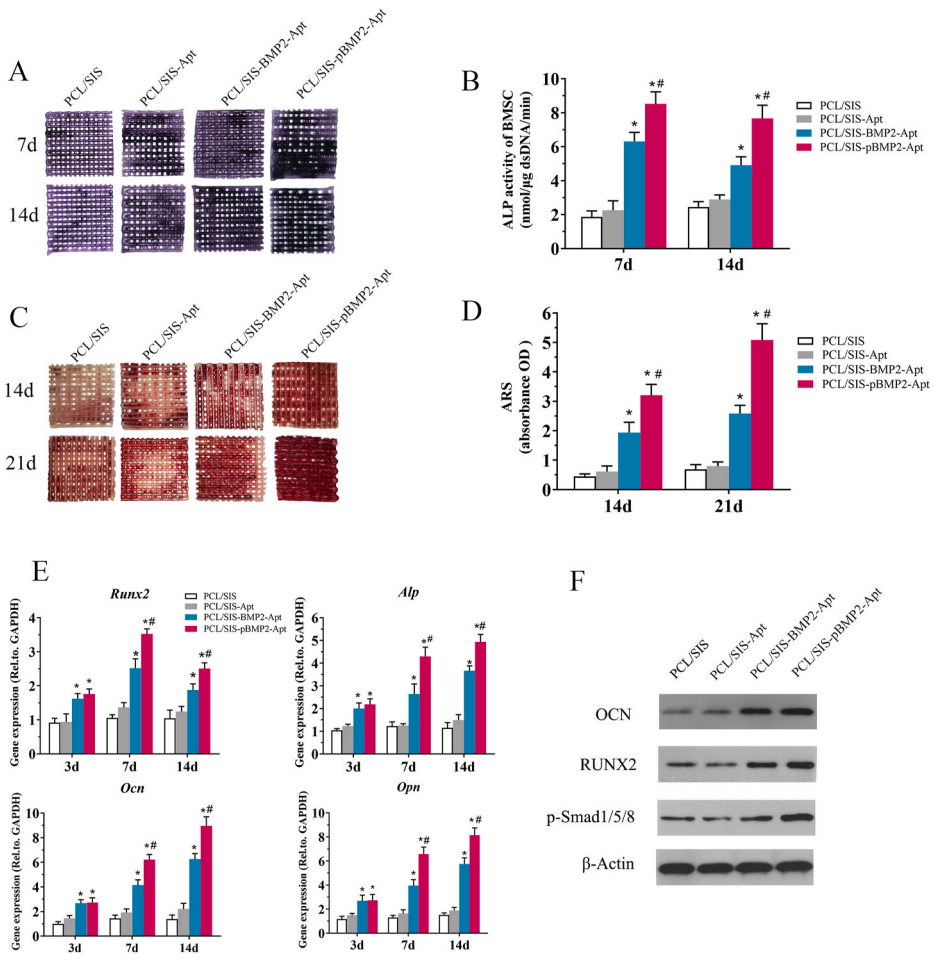

Fig. 6. Osteogenic differentiation analysis. (A) ALP staining of cells on PCL/SIS, PCL/SIS-Apt, PCL/SIS-BMP2-Apt and PCL/SIS-pBMP2-Apt scaffolds at days 7 and 14. (B) Quantification of ALP activity in cells on scaffolds at days 7 and 14. (C) ARS staining, a marker for minerals deposited by cells on scaffolds, at days 14 and 21. (D) Quantification of minerals deposited by cells on scaffolds at days 14 and 21. (E) Time course changes in mRNA expression of osteogenic markers, such as Runx-2, ALP, Ocn and Opn in cells on PCL/SIS, PCL/SIS-Apt, PCL/SIS-BMP2-Apt and PCL/SIS-pBMP2-Apt scaffolds after culture for 7 and 14 days. (F) Western blot analysis for the osteogenic markers, RUNX2 and OCN, and osteogenic-related signal pathway molecule (Smad 1/5/8) after culture for 7 days. ALP, alkaline phosphatase; ARS, Alizarin Red S. mRNA, messenger RNA; BMP2, bone morphogenetic protein 2; Ocn, osteocalcin; Opn, osteopontin; Statistical significance is indicated by $*p < 0.05$ compared with the PCL/SIS group and $\#p < 0.05$ compared with the PCL/SIS-BMP2-Apt group.

regeneration *in situ*, which sequentially delivered double factors in specific growth stages to enhance stem cells homing and colonization, as well as direct cell differentiation to osteogenic lineage. Apt19s was firstly released to enhance BMSC homing. Then, ECM super affinity peptide-fused BMP2 was sequentially delivered to stimulate the osteogenic differentiation of these BMSCs.

The two nozzles cryogenic free-form extrusion systems developed in our lab were used to print PCL and SIS at a low temperature. Compared to traditional 3D printing technology, cryogenic free-form extrusion was performed at −20 °C to retain the bioactivity of the bio-ink during fabrication to test for functionality under extreme conditions [27]. Polymer poly (ϵ-caprolactone) (PCL), an FDA-cleared and bioresorbable polymer, was co-printed as a backbone to support the 3D architecture, as the mechanical strength of this pure protein-based material is far away from that of native bone [25]. In previous studies, PCL was usually printed at or above 65 °C using traditional 3D technology, which does not allow for the co-printing of biologics during fabrication. Moreover, cryogenic printing allows the phase separation of liquid in bio-ink and PCL slurry. With the subsequent lyophilization, scaffolds have a higher porosity and a rougher surface. These physicochemical traits endow scaffolds with an excellent surface for cell adhesion, migration, and drug delivery.

In the present study, a sequential release system for Apt19s and BMP2 was designed to promote cell homing and the regulation of osteogenesis. To enhance bone regeneration, several researchers have previously attempted to co-deliver BMP2 and growth factors, including stromal-derived factor (SDF-1), platelet-derived growth factor (PDGF-BB), fibroblast growth factor (FGF-2), or vascular endothelial growth factor (VEGF) [32–35]. However, the simultaneous co-delivery of these growth factors was only found to moderately improve bone regeneration. In fact, PDGF-BB was even found to hinder the bone regeneration ability of co-delivered BMP2 [36], indicating the necessity for a sequential delivery strategy [37]. In the PCL/SIS-pBMP2-Apt system, Apta19s was released in a burst in the first day, followed by a slower release for 7 d, whereas pBMP2 was released in a smaller burst in the first day, followed by a substantially longer release for up to 4 weeks. In contrast, for the PCL/SIS-BMP2-Apt system, both Apt19s and BMP2 exhibited burst release in the first day and a shorter release for less than 2 weeks. The insertion of the PlGF-$2_{123\text{-}144}$ domain into pBMP2 conferred super-affinity for ECM proteins, which maintained a sustained release. According to previous studies, PlGF-$2_{123\text{-}144}$-fused growth factors resulted in 2- to 100-fold increases in affinity compared to the wild-type, depending on the particular growth factor [25,26].

Cell homing is fundamental in tissue regeneration [38,39]. Even if there is an inherent driving force recruiting endogenous stem cells to bone defects *in vivo*, the inflammatory context after severe damage may interfere with these processes [40]. Thus, enhancing the cell homing ability of BMSCs is a key process in bone repair [41,42]. In the present study, the results of the transwell assay demonstrated that the Apt19s significantly improved the number of migrated cells compared to the control group, as shown in Fig. 5A. Both the concomitant and sequential release of Apt19s and BMP2 generated a synergistic effect on cell migration. In a previous study, BMP2 was found to accelerate the migration of BMSCs via the CDC42/PAK1/LIMK1 pathway both *in vitro* and *in vivo* [43].

The *in vitro* effects of Apt19s and BMP2 on the proliferation and osteogenic differentiation of BMSCs were investigated. The addition of Apt19s alone was found to barely affect BMSCs proliferation, ALP

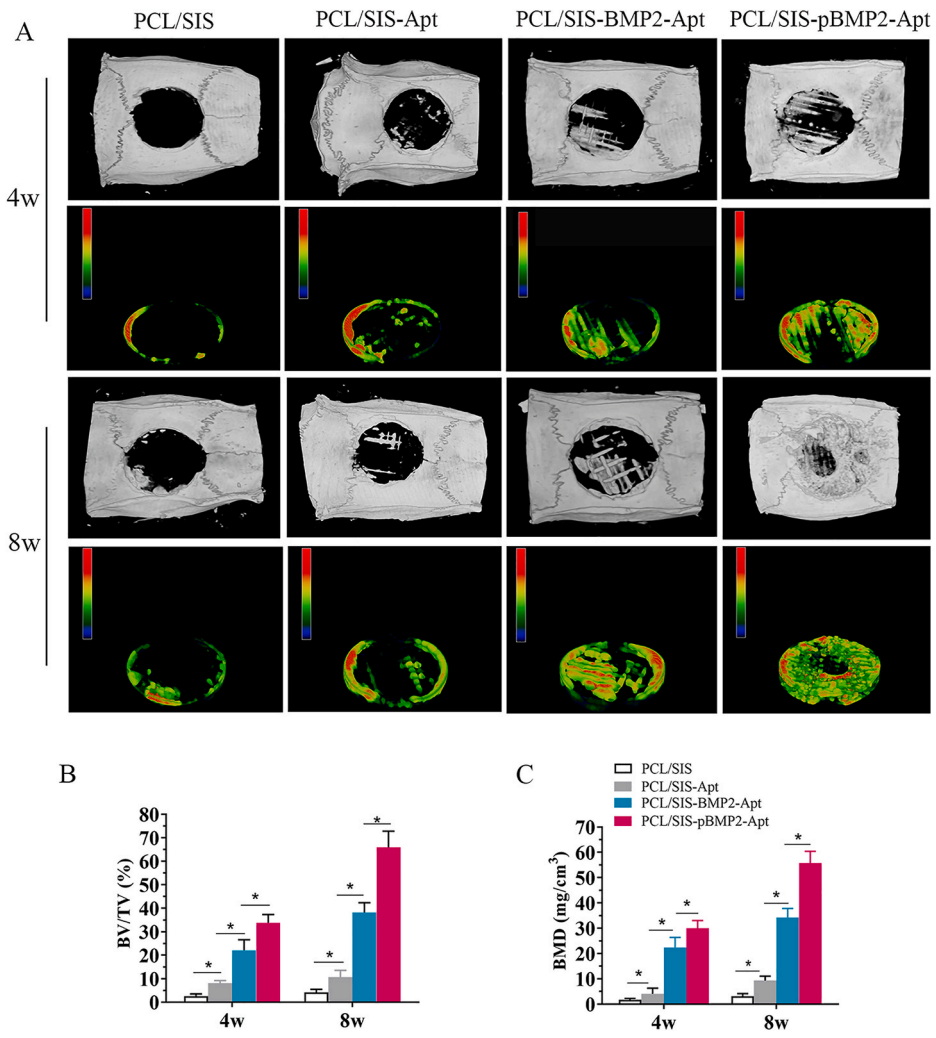

Fig. 7. Micro-CT evaluation of the repaired skull at 4 and 8 weeks after implantation. (A) Representative micro-CT images and pseudo-color images of calvarial defects treated with PCL/SIS, PCL/SIS-Apt, PCL/SIS-BMP2-Apt and PCL/SIS-pBMP2-Apt. (B) Quantitative analysis of bone volume fraction (BV/TV) in the repaired cranial defect area. (C) Quantitative analysis of BMD in the repaired cranial defect area. Statistical significance is indicated by $^{*}p < 0.05$. BV, bone volume; BMD, bone mineral density; TV, total volume.

activity, calcium nodule deposition, or the expression level of osteogenesis-related mRNA compared to the control group, suggesting that Apt19s alone is unable to enhance osteogenic differentiation *in vitro*. Scaffolds containing BMP2 exhibited remarkably improved cell proliferation and osteogenic differentiation compared to scaffolds without BMP2. However, the sequential release system of PCL/SIS-pBMP2-Apt induced stronger osteoblastic activity than the concomitant release system of PCL/SIS-BMP2-Apt over prolonged periods. In addition, it indicated that the incorporation of PlGF-$2_{123\text{-}144}$ peptide did not trigger detrimental effects on the bioactivity of BMP2 [26]. Osteogenesis-related genes were upregulated in the PCL/SIS-pBMP2-Apt group compared to the PCL/SIS or PCL/SIS groups. At the early time point of 3 d, no significant differences were detected between PCL/SIS-pBMP2-Apt and PCL/SIS-BMP2-Apt groups. However, after 7 and 14 d of culture, higher gene expression levels were detected in the PCL/SIS-pBMP2-Apt group compared to the PCL/SIS-BMP2-Apt group. In accordance with the results of the gene expression analysis, the expression levels of the osteogenic proteins, RUNX2, OCN, and *p*-Smad1/5/8 protein, were also elevated in PCL/SIS-pBMP2-Apt compared to the PCL/SIS-BMP2-Apt scaffold. Previous literature studies have reported that Smad1/5/8 is phosphorylated by type I receptors of BMP2 and translocates to the nucleus to activate osteogenic genes such as *runx2* and *ocn* [44,45]. Thus, it is reasonable to deduce that BMP2 released from PCL/SIS-pBMP2-Apt promoted the osteogenic differentiation via activation of the Smad1/5/8 pathway. Collectively, the sequential release system from the PCL/SIS-pBMP2-Apt scaffolds provided a more sustainable effect on the stimulation of osteogenic differentiation compared to the concomitant release system from the PCL/SIS-BMP2-Apt scaffolds.

To confirm the synergetic effect of aptamers and BMP2 on bone regeneration, a critical-sized calvarial defect model was used. As shown in Fig. 8A, mineralized tissue grew in a lattice shape. The PCL filaments acted as templates, guiding the mineralization and new bone formation, resulting in new bone formatted concomitantly with PCL filaments. By comparison with the *in vitro* results, the PCL/SIS scaffolds loaded with Apt19s alone significantly increased the bone volume compared to the pure PCL/SIS scaffolds. This may be attributed to the fact that Apt19s-directed stem cell recruitment has a positive effect on bone regeneration. Several studies have attempted to establish scaffolds with aptamers to evaluate their ability to recruit endogenous MSCs [46,47]. Thus, aptamer-directed stem cell enrichment is a promising potential method for tissue-engineering [48,49]. PCL/SIS-pBMP2-Apt was found to enhance bone regeneration in comparison to PCL/SIS-BMP2-Apt. We concluded that the sustained and slow release of BMP2 from the sequential release system of PCL/SIS-pBMP2-Apt induced a higher degree of bone formation than the concomitant release system of PCL/SIS-BMP2-Apt over prolonged periods. Moreover, histological results showed that no obvious immunological response or inflammatory signs were observed, despite SIS being derived from the porcine jejunum. The sequential release of these two bioactive molecules from scaffolds is profitable for the enhancement of bone regeneration, since the initial fast release of aptamer drives BMSCs homing to defect areas at

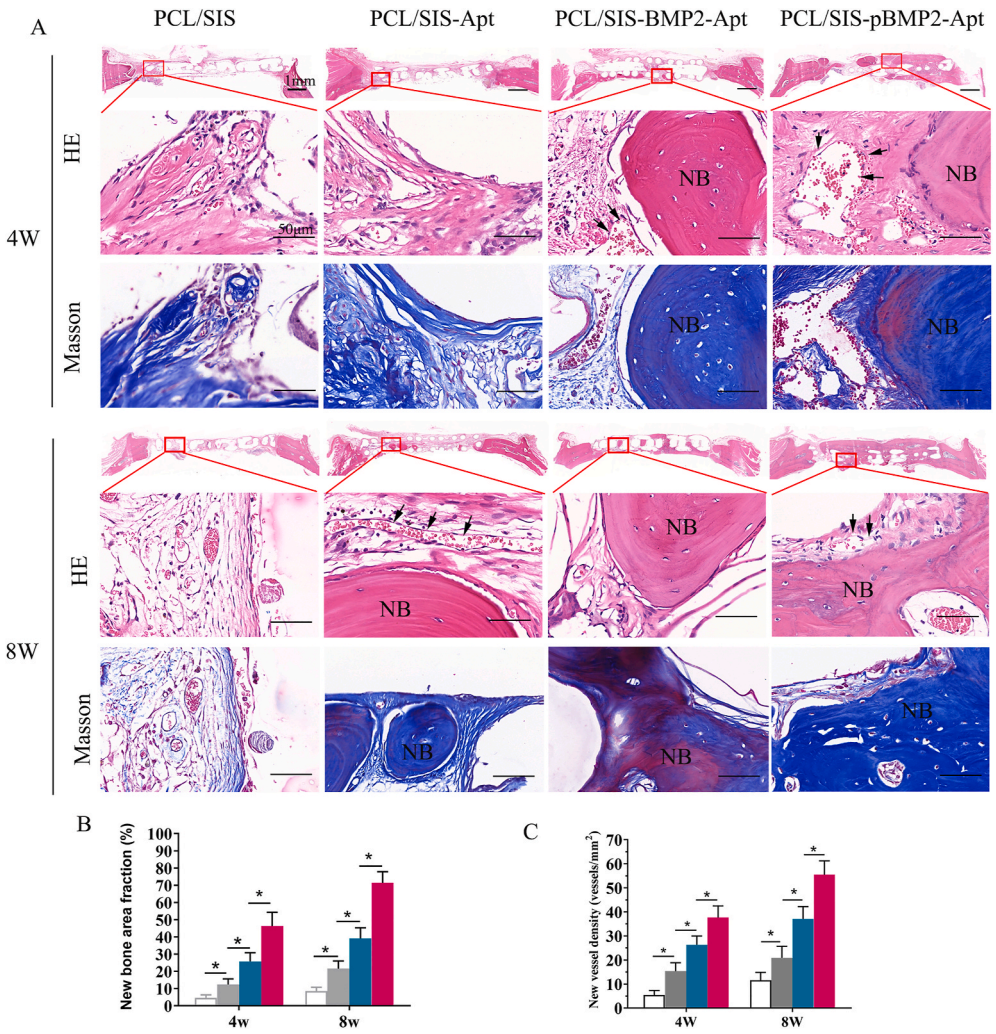

Fig. 8. Histological evaluations of cranial defect regeneration at 4 and 8 weeks post-implantation (A) Representative H&E and Masson staining histological images of PCL/SIS, PCL/SIS-Apt, PCL/SIS-BMP2-Apt and PCL/SIS-pBMP2-Apt. (B) Quantitative analysis of new bone area percentages. (C) Quantitative analysis of new vessel density in each group. NB represents newly formed bone. Black arrows represent vessels. Statistical significance is indicated by $^{*}p < 0.05$.

early stages, in addition to a sustained release of BMP2, which maintains an effective dose of BMP-2 to subsequently induce the osteogenic differentiation of BMSCs.

In the current study, we tried to initiate the endogenous mechanism to induce bone regeneration *in situ* using a sequential delivery system. The proposed system was composed of an ECM-based scaffold sequentially delivering Aptamer and an engineered BMP2. Compared with other chemokines, growth factors and aptamers, Apt19s could bind to endogenous BMSCs with a high affinity and selectivity, thus efficiently promoting cell homing. pBMP2 is fused with a domain of PlGF-$2_{123\text{-}144}$ peptide, which confers a "super affinity" to ECM-derived materials and possesses a controlled release profile from ECM-based delivery systems. Collectively, the novel PCL/SIS-pBMP2-Apt19s scaffold shows potential as an ideal alternative for successful stem cell mobilization and osteogenic differentiation, thus inducing bone regeneration *in situ*.

5. Conclusion

In situ guided bone regeneration is a promising approach for the regeneration of bone tissue and could be used to overcome the limitations of traditional bone tissue engineering, the latter of which typically involves extensive cell expansion steps, low cell survival rates upon transplantation, and a risk of immuno-rejection. Here, we presented a porous 3D PCL/SIS- pBMP2-Apt scaffold incorporating two factors to sequentially activate endogenous stem cell homing and osteogenic differentiation in two stages, ultimately achieving cell-free scaffold-based bone regeneration *in situ*. The first stage involved the release of Apt19s, which exhibited an excellent ability to promote the mobilization and recruitment of host BMSCs to defective sites in a large-scale bone defect model. In the second stage, BMP2 was released to induce BMSC osteogenic differentiation in a sustainable manner. Moreover, ECM-derived SIS proved to act as a profitable scaffold to guide BMSC adhesion, migration, and proliferation. Lastly, cryogenic free-form extrusion was developed to generate 3D constructs at low temperatures, thus enabling bio-inks to retain their bioactivity under extreme conditions.

CRediT authorship contribution statement

Tingfang Sun: Conceptualization, Original draft preparation, Funding acquisition. **Chunqing Meng:** Methodology, Writing – original draft, preparation. **Qiuyue Ding:** Investigation, Visualization, Methodology. **Keda Yu:** Investigation, Data curation. **Xianglin Zhang:** Resources, Visualization. **Wancheng Zhang:** Formal analysis, Software. **Wenqing Tian:** Methodology. **Qi Zhang:** Resources. **Xiaodong Guo:** Supervision, Project administration. **Bin Wu:** Resources, Methodology. **Zekang Xiong:** Supervision, Validation, Writing – review & editing.

Declaration of competing interest

No competing financial interests exist.

Acknowledgements

This research was financially supported by the National Natural Science Foundation of China (grant numbers 81902219, 81672158 and 81873999) and the National Key R&D Program of China (2016YFC1100100).

Appendix A. Supplementary data

Supplementary data to this article can be found online at https://doi.org/10.1016/j.bioactmat.2021.04.013.

References

[1] S.J. Wang, D. Jiang, Z.Z. Zhang, Y.R. Chen, Z.D. Yang, J.Y. Zhang, J. Shi, X. Wang, J.K. Yu, Biomimetic Nanosilica-Collagen Scaffolds for in Situ Bone Regeneration: toward a Cell-free, One-step Surgery, in: Advanced Materials, vol. 31, Deerfield Beach, Fla.), 2019, e1904341.

[2] W. Zhang, W. Shi, S. Wu, Kuss Ma, X. Jiang, J.B. Untrauer, S.P. Reid, B. Duan, 3D printed composite scaffolds with dual small molecule delivery for mandibular bone regeneration, Biofabrication (2020), https://doi.org/10.1088/1758-5090/ab906e.

[3] L. Zhang, G. Yang, B.N. Johnson, X. Jia, Three-dimensional (3D) printed scaffold and material selection for bone repair, Acta Biomater. 84 (2019) 16–33.

[4] Mandrycky Christian, Zongjie Wang, Keekyoung Kim, Kim Deok-Ho, 3D bioprinting for engineering complex tissues, Biotechnol. Adv. 34 (2016) 422–434.

[5] Aljohani Waeljumah, Ullah Muhammad Wajid, Xianglin Zhang, Guang Yang, Bioprinting and its applications in tissue engineering and regenerative medicine, Int. J. Biol. Macromol. 107 (2018) 261–275.

[6] M. Hospodiuk, D Sosnoski M Dey, I.T. Ozbolat, The bioink: a comprehensive review on bioprintable materials, Biotechnol. Adv. 35 (2017) 217–239.

[7] H. He, D. Li, Z. Lin, L. Peng, J. Yang, M. Wu, D. Cheng, H. Pan, C. Ruan, Temperature-programmable and enzymatically solidifiable gelatin-based bioinks enable facile extrusion bioprinting, Biofabrication (2020), https://doi.org/10.1088/1758-5090/ab9906.

[8] J. Hazur, R. Detsch, E. Karakaya, J. Kaschta, J. Tessmar, D. Schneidereit, O. Friedrich, D. Schubert, A.R. Boccaccini, Improving alginate printability for biofabrication: establishment of a universal and homogeneous pre-crosslinking technique, Biofabrication (2020), https://doi.org/10.1088/1758-5090/ab98e5.

[9] Y. Ji, J. Zhou, T. Sun, K. Tang, Z. Xiong, Z. Ren, S. Yao, K. Chen, F. Yang, F. Zhu, X. Guo, Diverse preparation methods for small intestinal submucosa (SIS): decellularization, components, and structure, J. Biomed. Mater. Res. 107 (2019) 689–697.

[10] Jinah Jang, Hun-Jun Park, Kim Seok-Won, Heejin Kim, Young Park Ju, Jin Na Soo, Ji Kim Hyeon, Nyeo Park Moon, Choi Seung Hyun, Hwa Park Sun, Won Kim Sung, Sang-Mo Kwon, Kim Pum-Joon, Cho Dong-Woo, 3D printed complex tissue construct using stem cell-laden decellularized extracellular matrix bioinks for cardiac repair, Biomaterials 112 (2017) 264–274.

[11] M. Hospodiuk, M. Dey, D. Sosnoski, I.T. Ozbolat, The bioink: a comprehensive review on bioprintable materials, Biotechnol. Adv. 35 (2017) 217–239.

[12] M.K. Kim, W. Jeong, S.M. Lee, J.B. Kim, S. Jin, H.W. Kang, Decellularized extracellular matrix-based bio-ink with enhanced 3D printability and mechanical properties, Biofabrication 12 (2020), 025003.

[13] M. Zhu, W. Li, X. Dong, X. Yuan, A.C. Midgley, H. Chang, Y. Wang, H. Wang, K. Wang, P.X. Ma, H. Wang, D. Kong, In vivo engineered extracellular matrix scaffolds with instructive niches for oriented tissue regeneration, Nat. Commun. 10 (2019) 4620.

[14] T. Sun, M. Liu, S. Yao, Y. Ji, Z. Xiong, K. Tang, K. Chen, H. Yang, X. Guo, Biomimetic composite scaffold containing small intestinal submucosa and mesoporous bioactive glass exhibits high osteogenic and angiogenic capacity, Tissue Eng. 24 (2018) 1044–1056.

[15] Lee Jong Seung, Yoonhee Jin, Hyun-Ji Park, Kisuk Yang, Min Suk Lee, Hee Seok Yang, Cho Seung-Woo, In situ bone tissue engineering with an endogenous stem cell mobilizer and osteoinductive nanofibrous polymeric scaffolds, Biotechnol. J. 12 (2017) 1700062.

[16] G. Wu, C. Feng, J. Quan, Z. Wang, W. Wei, S. Zang, S. Kang, G. Hui, X. Chen, Q. Wang, In situ controlled release of stromal cell-derived factor-1α and antimiR-138 for on-demand cranial bone regeneration, Carbohydr. Polym. 182 (2018) 215–224.

[17] S. Pacelli, S. Basu, J. Whitlow, A. Chakravarti, F. Acosta, A. Varshney, S. Modaresi, C. Berkland, A. Paul, Strategies to develop endogenous stem cell-recruiting bioactive materials for tissue repair and regeneration, Adv. Drug Deliv. Rev. 120 (2017) 50–70.

[18] JM WellsFM Watt, Diverse mechanisms for endogenous regeneration and repair in mammalian organs, Nature 557 (2018) 322–328.

[19] A. Malek-Khatabi, Javar Ha, E. Dashtimoghadam, S. Ansari, M.M. Hasani-Sadrabadi, A. Moshaverinia, In situ bone tissue engineering using gene delivery nanocomplexes, Acta Biomater. 108 (2020) 326–336.

[20] Z.W. Luo, F.X. Li, Y.W. Liu, S.S. Rao, H. Yin, J. Huang, C.Y. Chen, Y. Hu, Y. Zhang, Y.J. Tan, L.Q. Yuan, T.H. Chen, H.M. Liu, J. Cao, Z.Z. Liu, Z.X. Wang, H. Xie, Aptamer-functionalized exosomes from bone marrow stromal cells target bone to promote bone regeneration, Nanoscale 11 (2019) 20884–20892.

[21] X. Hu, Y. Wang, Y. Tan, J. Wang, H. Liu, Y. Wang, S. Yang, M. Shi, S. Zhao, Y. Zhang, Q. Yuan, A difunctional regeneration scaffold for knee repair based on aptamer-directed cell recruitment, Adv. Mater. 29 (2017).

[22] T. Sun, K. Zhou, M. Liu, X. Guo, Y. Qu, W. Cui, Z. Shao, X. Zhang, S. Xu, Loading of BMP-2-related peptide onto three-dimensional nano-hydroxyapatite scaffolds accelerates mineralization in critical-sized cranial bone defects, J Tissue Eng Regen Med 12 (2018) 864–877.

[23] C. Miao, D. Qin, P. Cao, P. Lu, Y. Xia, M. Li, M. Sun, W. Zhang, F. Yang, Y. Zhang, S. Tang, T. Liu, F. Liu, BMP2/7 heterodimer enhances osteogenic differentiation of rat BMSCs via ERK signaling compared with respective homodimers, J. Cell. Biochem. (2018), https://doi.org/10.1002/jcb.28162.

[24] K.W. Lo, B.D. Ulery, K.M. Ashe, C.T. Laurencin, Studies of bone morphogenetic protein-based surgical repair, Adv. Drug Deliv. Rev. 64 (2012) 1277–1291.

[25] Zekang Xiong, Wei Cui, Tingfang Sun, Yu Teng, Yanzhen Qu, Yang Liang, Jinge Zhou, Kaifang Chen, Sheng Yao, Zengwu Shao, Xiaodong Guo, Sustained delivery of PlGF-2123-144*-fused BMP2-related peptide P28 from small intestinal submucosa/polylactic acid scaffold material for bone tissue regeneration, RSC Adv. 10 (2020) 7289–7300.

[26] M.M. Martino, P.S. Briquez, E. Güç, F. Tortelli, W.W. Kilarski, S. Metzger, J.J. Rice, G.A. Kuhn, R. Müller, Swartz Ma, J.A. Hubbell, Growth factors engineered for super-affinity to the extracellular matrix enhance tissue healing, Science (New York, N.Y.) 343 (2014) 885–888.

[27] L. Shi, Y. Hu, M.W. Ullah, I. Ullah, H. Ou, W. Zhang, L. Xiong, X. Zhang, Cryogenic free-form extrusion bioprinting of decellularized small intestinal submucosa for potential applications in skin tissue engineering, Biofabrication 11 (2019), 035023.

[28] W.C. Zhang, I. Ullah, L. Shi, Y. Zhang, H. Ou, J.G. Zhou, M.W. Ullah, X.L. Zhang, W. C. Li, Fabrication and characterization of porous polycaprolactone scaffold via extrusion-based cryogenic 3D printing for tissue engineering, Mater. Des. 180 (2019) 10.

[29] T. Elzein, M. Nasser-Eddine, C. Delaite, S. Bistac, P. Dumas, FTIR study of polycaprolactone chain organization at interfaces, J. Colloid Interface Sci. 273 (2004) 381–387.

[30] T. Sun, Y. Qu, W. Cui, L. Yang, Y. Ji, W. Yu, R. Navinduth, Z. Shao, H. Yang, X. Guo, Evaluation of osteogenic inductivity of a novel BMP2-mimicking peptide P28 and P28-containing bone composite, J. Biomed. Mater. Res. 106 (2018) 210–220.

[31] J.R. Dias, N. Ribeiro, S. Baptista-Silva, A.R. Costa-Pinto, N. Alves, A.L. Oliveira, In situ enabling approaches for tissue regeneration: current challenges and new developments, Frontiers in bioengineering and biotechnology 8 (2020) 85.

[32] H. Wang, Q. Zou, O.C. Boerman, A.W. Nijhuis, J.A. Jansen, Y. Li, S. C. Leeuwenburgh, Combined delivery of BMP-2 and bFGF from nanostructured colloidal gelatin gels and its effect on bone regeneration in vivo, J. Contr. Release 166 (2013) 172–181.

[33] Bin Wang, Yuanwei Guo, Xiaofeng Chen, Chao Zeng, Qikang Hu, Wei Yin, Wei Li, Hui Xie, Bingyu Zhang, Xingchun Huang, Fenglei Yu, Nanoparticle-modified chitosan-agarose-gelatin scaffold for sustained release of SDF-1 and BMP-2, Int. J. Nanomed. 13 (2018) 7395–7408.

[34] Jie Yin, Sujun Qiu, Benchao Shi, Xiaolong Xu, Yunfei Zhao, Junhuai Gao, Shengli Zhao, Shaoxiong Min, Controlled release of FGF-2 and BMP-2 in tissue engineered periosteum promotes bone repair in rats, Biomed. Mater. 13 (2018), 025001.

[35] M. Sukul, T.B. Nguyen, Y.K. Min, S.Y. Lee, B.T. Lee, Effect of local sustainable release of BMP2-VEGF from nano-cellulose loaded in sponge biphasic calcium phosphate on bone regeneration, Tissue Eng. 21 (2015) 1822–1836.

[36] P.S. Lienemann, Q. Vallmajo-Martin, P. Papageorgiou, U. Blache, S. Metzger, A. S. Kivelio, V. Milleret, A. Sala, S. Hoehnel, A. Roch, R. Reuten, M. Koch, O. Naveiras, F.E. Weber, W. Weber, M.P. Lutolf, M. Ehrbar, Smart hydrogels for the augmentation of bone regeneration by endogenous mesenchymal progenitor cell recruitment, Advanced Science 7 (2020) 16.

[37] X. Shen, Y. Zhang, Y. Gu, Y. Xu, Y. Liu, B. Li, L. Chen, Sequential and sustained release of SDF-1 and BMP-2 from silk fibroin-nanohydroxyapatite scaffold for the enhancement of bone regeneration, Biomaterials 106 (2016) 205–216.

[38] M. Herrmann, S. Verrier, M. Alini, Strategies to stimulate mobilization and homing of endogenous stem and progenitor cells for bone tissue repair, Front Bioeng Biotechnol 3 (2015) 79.

[39] F.M. Chen, L.A. Wu, M. Zhang, R. Zhang, H.H. Sun, Homing of endogenous stem/progenitor cells for in situ tissue regeneration: promises, strategies, and translational perspectives, Biomaterials 32 (2011) 3189–3209.

[40] S.S. Jin, D.Q. He, D. Luo, Y. Wang, M. Yu, B. Guan, Y. Fu, Z.X. Li, T. Zhang, Y. H. Zhou, C.Y. Wang, Y. Liu, A biomimetic hierarchical nanointerface orchestrates macrophage polarization and mesenchymal stem cell recruitment to promote endogenous bone regeneration, ACS Nano 13 (2019) 6581–6595.

[41] L. Roseti, V. Parisi, M. Petretta, C. Cavallo, G. Desando, I. Bartolotti, B. Grigolo, Scaffolds for bone tissue engineering: state of the art and new perspectives, Mater Sci Eng C Mater Biol Appl 78 (2017) 1246–1262.

[42] Q. Chen, C. Zheng, Y. Li, S. Bian, H. Pan, X. Zhao, W.W. Lu, Bone targeted delivery of SDF-1 via alendronate functionalized nanoparticles in guiding stem cell migration, ACS Appl. Mater. Interfaces 10 (2018) 23700–23710.

[43] S. Liu, Y. Liu, L. Jiang, Z. Li, S. Lee, C. Liu, J. Wang, J. Zhang, Recombinant human BMP-2 accelerates the migration of bone marrow mesenchymal stem cells via the CDC42/PAK1/LIMK1 pathway in vitro and in vivo, Biomater Sci 7 (2018) 362–372.

[44] V.S. Salazar, L.W. Gamer, V. Rosen, BMP signalling in skeletal development, disease and repair, Nat. Rev. Endocrinol. 12 (2016) 203–221.
[45] D. Chen, M. Zhao, G.R. Mundy, Bone morphogenetic proteins, Growth Factors 22 (2004) 233–241.
[46] M. Wang, H. Wu, Q. Li, Y. Yang, F. Che, G. Wang, L. Zhang, Novel aptamer-functionalized nanoparticles enhances bone defect repair by improving stem cell recruitment, Int. J. Nanomed. 14 (2019) 8707–8724.
[47] X. Wang, X. Song, T. Li, J. Chen, G. Cheng, L. Yang, C. Chen, Aptamer-Functionalized bioscaffold enhances cartilage repair by improving stem cell recruitment in osteochondral defects of rabbit knees, Am. J. Sports Med. 47 (2019) 2316–2326.
[48] N. Ardjomandi, J. Huth, D.R. Stamov, A. Henrich, C. Klein, H.P. Wendel, S. Reinert, D. Alexander, Surface biofunctionalization of beta-TCP blocks using aptamer 74 for bone tissue engineering, Mater Sci Eng C Mater Biol Appl 67 (2016) 267–275.
[49] X. Wang, X. Zheng, Y. Duan, L. Ma, C. Gao, Defined substrate by aptamer modification with the balanced properties of selective capture and stemness maintenance of mesenchymal stem cells, ACS Appl. Mater. Interfaces 11 (2019) 15170–15180.